Hydra: Exploiting Multi-Bounce Scattering for Beyond-Field-of-View mmWave Radar

Nishant Mehrotra
Rice University
Houston, TX, USA
nm30@rice.edu

Divyanshu Pandey
Rice University
Houston, TX, USA
dp76@rice.edu

Akarsh Prabhakara
Carnegie Mellon University
Pittsburgh, PA, USA
aprabhak@andrew.cmu.edu

Yawen Liu
Carnegie Mellon University
Pittsburgh, PA, USA
yawenl@andrew.cmu.edu

Swarun Kumar
Carnegie Mellon University
Pittsburgh, PA, USA
swarun@cmu.edu

Ashutosh Sabharwal
Rice University
Houston, TX, USA
ashu@rice.edu

ABSTRACT

In this paper, we ask, "Can millimeter-wave (mmWave) radars sense objects not directly illuminated by the radar – for instance, objects located outside the transmit beamwidth, behind occlusions, or placed fully behind the radar?" Traditionally, mmWave radars are limited to sense objects that are directly illuminated by the radar and scatter its signals directly back. In practice, however, radar signals scatter to other intermediate objects in the environment and undergo multiple bounces before being received back at the radar. In this paper, we present Hydra, a framework to explicitly model and exploit multi-bounce paths for sensing. Hydra enables standalone mmWave radars to sense beyond-field-of-view objects without prior knowledge of the environment. We extensively evaluate the localization performance of Hydra with an off-the-shelf mmWave radar in five different environments with everyday objects. Exploiting multi-bounce via Hydra provides 2×-10× improvement in the median beyond-field-of-view localization error over baselines.

CCS CONCEPTS

• **Hardware** → **Digital signal processing**; **Sensor applications and deployments**; • **Computer systems organization** → *Sensor networks.*

KEYWORDS

millimeter-wave, multi-bounce scattering, radar, sensing

ACM MobiCom '24, November 18–22, 2024, Washington D.C., DC, USA

ACM ISBN 979-8-4007-0489-5/24/11.
https://doi.org/10.1145/3636534.3690710

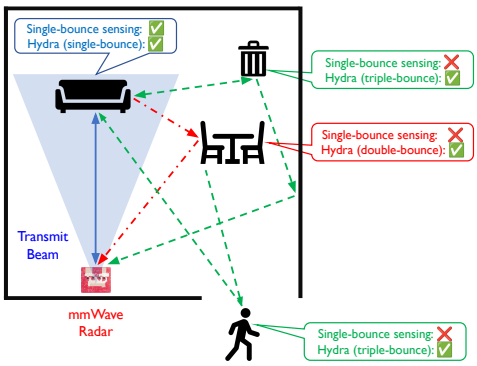

Figure 1: Hydra utilizes multi-bounce scattering for mmWave sensing of objects that are otherwise not detected by conventional single-bounce sensing methods.

ACM Reference Format:
Nishant Mehrotra, Divyanshu Pandey, Akarsh Prabhakara, Yawen Liu, Swarun Kumar, and Ashutosh Sabharwal. 2024. Hydra: Exploiting Multi-Bounce Scattering for Beyond-Field-of-View mmWave Radar. In *The 30th Annual International Conference on Mobile Computing and Networking (ACM MobiCom '24), November 18–22, 2024, Washington D.C., DC, USA.* ACM, New York, NY, USA, 15 pages. https://doi.org/10.1145/3636534.3690710

1 INTRODUCTION

Millimeter-wave (mmWave) radars are an emerging sensing modality being used in various applications such as autonomous driving [13, 36], security [30, 37], non-destructive evaluation [31, 33], spatial computing [23], indoor navigation [26], and beyond. Their larger bandwidths enable better ranging accuracy, and their unique depth penetration abilities enable sensing through visible light occlusions, such as fog [13] and smoke [26], as well as in the dark [30].

However, traditional radar processing is limited to sense objects that are directly illuminated by the radar and that scatter radar illumination directly back. We call such methods

single-bounce sensing, and a large class of the literature [13–15, 26, 32, 34, 48, 51–53] falls under this category. In practice, however, a large fraction of incident illumination is scattered to other intermediate objects in the environment, and radar signals undergo *multiple bounces* before being received back at the radar. This leads us to ask, "Is it possible to exploit such multi-bounce scattering paths to sense objects that are not directly illuminated by the radar?"

In this paper, we propose Hydra[1], a novel framework that exploits multi-bounce scattering to enable mmWave sensing of objects that are not directly illuminated by the radar, and hence not are detected by conventional single-bounce methods. An example scenario is depicted in Fig. 1, where only the sofa is directly illuminated by the radar and hence is detected via single-bounce, but all other objects (dining furniture, trashcan and behind-radar human) are not detected. In the sequel, we refer to all objects not directly illuminated by the radar as *beyond field-of-view* objects, since they lie outside the radar's field-of-view (FoV), i.e., transmit beam.

Sensing beyond-FoV objects, e.g., behind the radar or around corners, is crucial in scenarios such as navigation and traffic scheduling at intersections, intrusion detection in smart homes, etc. Prior solutions to sense beyond-FoV objects leverage system mobility [26, 32, 34, 45, 51, 52] and/or multiple modules - 2+ radars [42, 49] or radar + lidar [36, 46, 50] (see Section 2 for a review of related work). Hydra is a complementary solution that enables *standalone* mmWave radars to sense beyond-FoV objects purely purely using computational resources at no additional cost - making Hydra attractive in scenarios where hardware size/cost is at a premium, e.g., low form factor drones, roadside infrastructure units, etc. Moreover, Hydra requires no prior knowledge of the environment unlike prior beyond-FoV sensing solutions that require knowledge of key reflectors.

There are two main challenges associated with the design of Hydra. First, with no prior knowledge of objects in the environment, it is unclear how the radar should transform its measurements to spatial locations in the environment. Second, it is well-known that the received power of multi-bounce decays with each additional bounce [1]. Hence, detecting beyond-FoV objects from the combination of single-, double- and triple-bounce paths received at the radar is challenging because single-bounce paths typically greatly dominate in power over double- and triple-bounce paths.

As a key intermediate step towards solving the first challenge, we mathematically model diffuse multi-bounce scattering from objects. Our modeling insights lead to a matched filtering algorithm that directly localizes objects to their ground-truth locations along specific multi-bounce paths. To solve the second challenge, we perform matched filtering and object detection *separately & sequentially* along single-, double- and triple-bounce. For each multi-bounce order, object detection is performed via a custom ordered statistics constant false alarm rate detector (OS-CFAR) [35], and objects detected in lower multi-bounce orders are used as *anchors* to localize objects in undetected regions of the environment with higher-order multi-bounce. For example, in the context of Fig. 1, the sofa is first localized via single-bounce, and is used to subsequently localize the dining furniture via double-bounce. The process is repeated to sense the behind-radar human and occluded trashcan via triple-bounce paths. We do not utilize fourth- and higher-order bounces since empirically we find the power of such paths too low to exploit.

We implement Hydra on a commercial digital mmWave multiple-input multiple-output (MIMO) radar testbed (TI AWR2243 cascade radar [18]), and extensively evaluate its performance in five different indoor and outdoor scenarios, and exploit multi-bounce paths from a wide variety of everyday objects and surfaces, including human bodies, indoor furniture, and extended room and building features. We demonstrate that even with no prior knowledge of the environment, modeling and exploiting double-bounce and triple-bounce paths can improve the median localization error for human targets standing outside the radar's field-of-view by 2×-10× over traditional single-bounce methods.

In summary, our main contributions are as follows:

- We propose Hydra, a framework that models and exploits diffuse multi-bounce scattering to enable beyond-field-of-view sensing with a single mmWave radar without prior knowledge of the environment.
- We propose a sequential procedure that: (i) performs matched filtering and target detection separately and sequentially over different orders of multi-bounce, and (ii) uses target detections from previous iterations as anchors to localize objects along multiple possible multi-bounce paths of a given order.
- Our implementation on a commercial digital mmWave MIMO radar (TI AWR2243 cascade radar [18]) demonstrates 2×-10× improvement in the median localization error for humans standing outside the radar's field-of-view across 5 different indoor and outdoor scenarios, exploiting multi-bounce from a wide variety of everyday objects and surfaces, such as human bodies, indoor furniture, and extended room and building features.

We note that our design is limited to sensing static objects in the range-azimuth plane, and is not fully optimized in terms of its computational complexity. Our objective in this paper is to experimentally demonstrate and benchmark the underlying principles of beyond-field-of-view sensing with standalone mmWave radars. We discuss the limitations of our design and describe potential extensions in Section 6.

[1]named after the multi-headed Greek mythological monster

Reference	Environment Knowledge	Additional Hardware		Multi-Bounce Order		
		Lidar	Reflector	Single	Double	Triple
[36, 46, 50]	✓	✓	×	×	×	✓
[2, 39, 44]	✓	×	✓	×	×	✓
[6, 12, 16, 21, 22]	✓	×	×	✓	✓	✓
This Work	×	×	×	✓	✓	✓

Table 1: `Hydra` exploits multi-bounce scattering to enable a single mmWave radar to sense beyond its field-of-view without prior knowledge of the environment or additional hardware such as dedicated reflectors or lidars.

The next section summarizes related work. Section 3 describes the limitations of single-bounce sensing, which inform `Hydra`'s design in Section 4. Section 5 evaluates `Hydra`'s performance across 5 different indoor and outdoor settings. We conclude the paper in Section 7 after discussing the limitations of our design and future work in Section 6.

2 RELATED WORK

Table 1 summarizes the related work discussed below.

Single-bounce sensing: Traditional mmWave sensing algorithms only model single-bounce reflections from the environment [13–15, 26, 32, 34, 48, 51–53]. However, mmWave signal directionality limits the single-bounce FoV to non-occluded objects within the transmit beam. Existing solutions sense in a wider FoV via: (i) beam scanning [11, 14, 15, 53], (ii) multiple radars to span the entire 360° FoV around the system [42, 49], or (iii) system rotation and mobility [26, 32, 34, 45, 51, 52]. `Hydra` complements these methods by enabling standalone mmWave radars to sense beyond-FoV objects without additional hardware, even when the radar is static.

Around-corner sensing: There exists rich literature on around-corner radar sensing [2, 36, 39, 44, 46, 50], inspired from similar ideas in visible light and acoustic imaging [9, 24, 25, 41]. However, the scenarios considered only consist of triple-bounce paths. Traditional around-corner approaches process the triple-bounce data with single-bounce algorithms, resulting in "ghosts" (mirror images) of objects about reflectors in the environment (walls, etc.). Subsequently, *prior knowledge* of the environment – via dedicated reflectors [2, 39, 44] or lidar-based environment mapping [36, 46, 50] – is used to "remap" the ghosts to their ground-truth locations. However, such approaches are environment-specific and increase the overall hardware complexity and cost. `Hydra` explores the general problem of beyond-FoV sensing with a *single* mmWave radar via double-bounce and triple-bounce paths *without* prior environment knowledge.

Multi-bounce exploitation: The general problem of sensing with arbitrary multi-bounce has been considered in [6, 10, 12, 16, 20–22, 27, 28]. Similar to around-corner sensing, the common approach is to use single-bounce sensing models, resulting in the formation of multipath "ghosts", which must first be identified, e.g., via range-Doppler characteristics [10], and subsequently suppressed [6, 10, 21] or remapped to their ground-truth locations [5, 12, 20]. By modeling multi-bounce scattering, `Hydra` avoids the need for "ghost" identification and suppression/remapping.

Channel estimation & localization: Our work is also broadly related to WiFi/mmWave channel estimation [19, 45], which is used to localize devices [4, 7, 22, 40, 43]. The major differences of [4, 7, 19, 22, 40, 43, 45] with `Hydra` are: (i) they localize RF-enabled radios or RFID tags whereas `Hydra` localizes non-RF enabled objects, (ii) they are limited to exploiting single-bounce paths that bounce once in the environment, whereas `Hydra` uses n-bounce scattering, for $n \geq 1$.

Programmable surfaces to aid sensing: Finally, recent work [3, 29, 47] explores deploying *programmable surfaces* to improve sensing performance. Since `Hydra` focuses on exploiting natural multi-bounce in the environment, such systems are beyond the scope of this present work but present an interesting exploration space for future work.

3 SINGLE-BOUNCE FOV LIMITATIONS

We begin by modeling single-bounce sensing with MIMO radars, and show that the single-bounce field-of-view is inherently limited to the transmit beampattern of the system. The FoV limitations of single-bounce are subsequently used to inform the multi-bounce design of `Hydra` in Section 4.

3.1 MIMO Radar System Model

Consider a digital mmWave MIMO radar equipped with T transmit and R receive elements. The radar remains static, transmit beamforms in a fixed direction with $\mathsf{T} \times 1$ transmit beamforming weights $\mathbf{w}_{\text{TX}}$, and captures reflections from the surrounding static environment. For simplicity, we only model the range and azimuth angles, and not elevation.

The time-domain transmitted signals can be written as a $\mathsf{T} \times 1$ vector, $\mathbf{x}(t) = \mathbf{w}_{\text{TX}} x(t)$, for a complex scalar transmit waveform $x(t)$. The $\mathsf{R} \times 1$ vector of time-domain received signals is given by the sum of attenuated and delayed copies of $\mathbf{x}(t)$ along different paths ℓ, weighted by $\mathsf{T} \times 1$ transmit

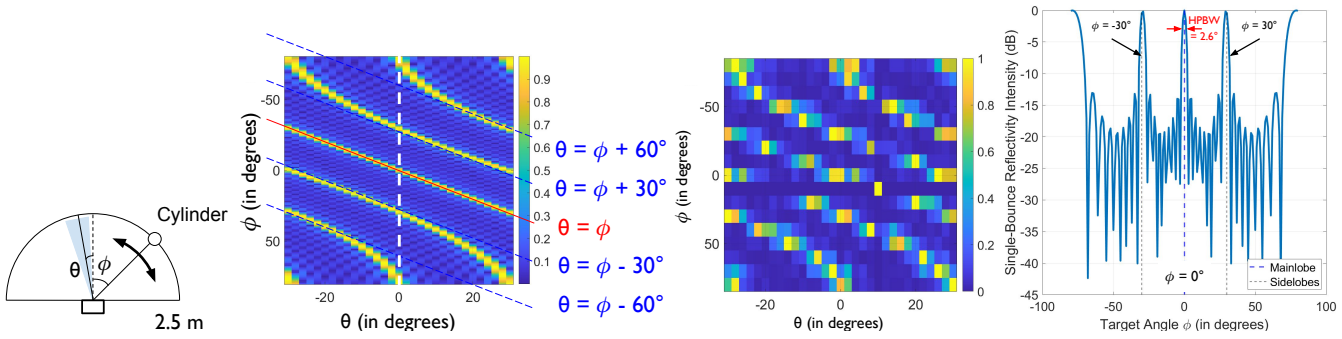

(a) Experiment setup **(b) Simulation result** **(c) Experimental result** **(d) TX beampattern ($\theta = 0°$)**

Figure 2: Experiment to evaluate sensing FoV with single-bounce. (a) Setup. (b)-(d): Normalized single-bounce reflectivity magnitudes from (4) show that single-bounce FoV is limited to main- and side-lobes of transmit array.

and R × 1 receive steering vectors, $\mathbf{a}_{\text{TX}}(\theta^{\ell}_{\text{TX}})$ and $\mathbf{a}_{\text{RX}}(\theta^{\ell}_{\text{RX}})$, corresponding to each path's angle-of-departure and arrival,

$$\mathbf{y}(t) = \sum_{\ell} \alpha_{\ell} \mathbf{a}_{\text{RX}}(\theta^{\ell}_{\text{RX}}) \mathbf{a}^{\top}_{\text{TX}}(\theta^{\ell}_{\text{TX}}) \mathbf{w}_{\text{TX}} x(t - \tau_{\ell}), \tag{1}$$

where α_{ℓ} and τ_{ℓ} model attenuation and time delay of path ℓ, $(\cdot)^{\top}$ denotes transpose, and we have ignored noise and the frequency dependence of the steering vectors.

Consider single-bounce paths of the form: radar $\rightarrow \mathbf{p} \rightarrow$ radar, for locations $\mathbf{p} \in \mathbb{R}^2$ in the environment. The angles-of-departure and arrival are equal for such paths, i.e., $\theta^{\ell}_{\text{TX}} = \theta^{\ell}_{\text{RX}} = \theta_{\mathbf{p}}$, where $\theta_{\mathbf{p}}$ denotes the azimuth angle of $\mathbf{p}$ with respect to the radar (assumed at origin). The time delay corresponds to the round-trip delay to location $\mathbf{p}$, i.e., $\tau_{\ell} = \frac{2\|\mathbf{p}\|_2}{c}$, for speed of light c. Furthermore, $\alpha_{\ell} = \sigma_{\mathbf{p}}$ is the path attenuation due to the combined effect of the reflectivity and path loss to-and-from $\mathbf{p}$. Hence, (1) for single-bounce paths is

$$\mathbf{y}_{\text{SB}}(t) = \sum_{\mathbf{p}} \sigma_{\mathbf{p}} \mathbf{a}_{\text{RX}}(\theta_{\mathbf{p}}) \mathbf{a}^{\top}_{\text{TX}}(\theta_{\mathbf{p}}) \mathbf{w}_{\text{TX}} x\left(t - \frac{2\|\mathbf{p}\|_2}{c}\right). \tag{2}$$

3.2 Single-Bounce Sensing Pipeline

The goal of sensing is to estimate reflectivities $\sigma_{\mathbf{p}}$ given the measurements $\mathbf{y}_{\text{SB}}(t)$ and transmit signal $x(t)$ (known to the radar); non-zero magnitudes of $\sigma_{\mathbf{p}}$ indicate presence of an object at location $\mathbf{p}$. After matched filtering with $x(t)$, the system model may be expressed in the frequency domain as

$$\tilde{\mathbf{y}}_{\text{SB}}(\omega) = \sum_{\mathbf{p}} \sigma_{\mathbf{p}} \mathbf{a}_{\text{RX}}(\theta_{\mathbf{p}}) \mathbf{a}^{\top}_{\text{TX}}(\theta_{\mathbf{p}}) \mathbf{w}_{\text{TX}} e^{-j\omega \frac{2\|\mathbf{p}\|_2}{c}}. \tag{3}$$

A common approach to estimate $\sigma_{\mathbf{p}}$ from $\tilde{\mathbf{y}}_{\text{SB}}(\omega)$ in (3) is via *adjoint inversion* (also called back-projection) [8, 38],

$$\hat{\sigma}_{\mathbf{p}} = \frac{1}{\text{W}} \sum_{\omega} \left(\mathbf{a}^{\top}_{\text{TX}}(\theta_{\mathbf{p}}) \mathbf{w}_{\text{TX}}\right)^{*} e^{j\omega \frac{2\|\mathbf{p}\|_2}{c}} \mathbf{a}^{\text{H}}_{\text{RX}}(\theta_{\mathbf{p}}) \tilde{\mathbf{y}}_{\text{SB}}(\omega), \tag{4}$$

where $(\cdot)^{*}$ and $(\cdot)^{\text{H}}$ denote the complex conjugate and Hermitian operations, and W is the total number of frequencies considered. The estimator in (4) has a simple interpretation: *receive beamform* to locations $\mathbf{p}$ (via $\mathbf{a}^{\text{H}}_{\text{RX}}(\theta_{\mathbf{p}})\tilde{\mathbf{y}}_{\text{SB}}(\omega)$), followed by *matched filtering* to kernel $\mathbf{a}^{\top}_{\text{TX}}(\theta_{\mathbf{p}})\mathbf{w}_{\text{TX}} e^{-j\omega \frac{2\|\mathbf{p}\|_2}{c}}$, which is known since a co-located receiver knows the transmit beamformer $\mathbf{w}_{\text{TX}}$ and distances $\|\mathbf{p}\|_2$ to locations $\mathbf{p}$.

3.3 Single-Bounce Limits Sensing FoV

We now theoretically and experimentally demonstrate that the sensing FoV with single-bounce-only processing is limited to the main- and side-lobes of the transmit array. To that end, note that as per (2), single-bounce scattering from a location $\mathbf{p}$ is non-zero if the following condition holds:

$$\|\mathbf{a}_{\text{RX}}(\theta_{\mathbf{p}}) \mathbf{a}^{\top}_{\text{TX}}(\theta_{\mathbf{p}}) \mathbf{w}_{\text{TX}}\|_2 > 0. \tag{5}$$

Assuming the receive array steering vector $\mathbf{a}_{\text{RX}}(\theta_{\mathbf{p}})$ has unit-norm, (5) simplifies to $|\mathbf{a}^{\top}_{\text{TX}}(\theta_{\mathbf{p}})\mathbf{w}_{\text{TX}}| > 0$, where $|\cdot|$ indicates magnitude. The condition holds for all locations within the *main- and side-lobes* of the radar's transmit beampattern.

We illustrate the above concept via a simple range-azimuth domain simulation and experiment with a TI mmWave MIMO radar [18], with 9- and 16-element transmit and receive uniform linear arrays (per-element spacing: 2λ (transmit), 0.5λ (receive), for wavelength λ). The simulated and experimental setup is shown in Fig. 2(a). We configure the radar to transmit beamform towards an azimuth angle $\theta \in [-30°, +30°]$, hence $\mathbf{w}_{\text{TX}} = \mathbf{a}_{\text{TX}}(\theta)$. For each transmit angle, we capture reflections for different azimuth angle locations $\phi \in [-80°, +80°]$ of a metallic cylinder[2] at 2.5 m range in front of the radar. Subsequently, the magnitude of the reflectivity estimate $\hat{\sigma}_{\mathbf{p}(\phi)}$ at the cylinder's ground-truth location $\mathbf{p}(\phi)$ is visualized across all combinations of (ϕ, θ) as a 2D matrix. Each element of the matrix (derivation in Appendix A) corresponds to:

$$|\hat{\sigma}_{\mathbf{p}(\phi)}| = |\sigma_{\mathbf{p}(\phi)}| |\mathbf{a}^{\top}_{\text{TX}}(\phi) \mathbf{a}_{\text{TX}}(\theta)|^2, \tag{6}$$

i.e., squared left-hand side of (5) with $\theta_{\mathbf{p}} = \phi$, $\mathbf{w}_{\text{TX}} = \mathbf{a}_{\text{TX}}(\theta)$, scaled by the ground-truth cylinder reflectivity $|\sigma_{\mathbf{p}(\phi)}|$.

[2] acts as a highly reflective omnidirectional (diffuse) scatterer

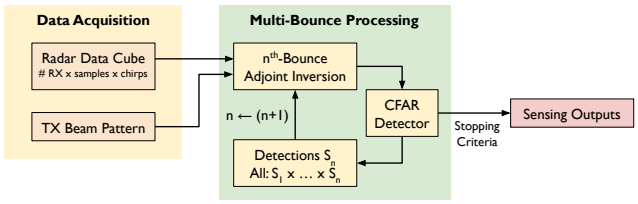

Figure 3: System overview of Hydra.

Figs. 2(b)-(c) show the simulated and experimental matrices, with each row normalized to its maximum value to remove the scaling factor $|\sigma_{\mathbf{p}(\phi)}|$. We observe that matrix entries have a high magnitude roughly when $\phi = \theta \pm m \times 30°$, for any positive integer m, which correspond to the main- and side-lobes of the transmit beampattern, also shown in Fig. 2(d) for $\theta = 0°$. Note that the side-lobes arise due to the 2λ spacing at the transmit array. The good match between theory and experiment validates our claim that single-bounce limits the sensing FoV to the system's transmit beampattern.

4 SYSTEM DESIGN: HYDRA

With the understanding that single-bounce limits the sensing FoV, we design Hydra to enable a single mmWave radar to sense beyond its single-bounce FoV via natural multi-bounce scattering, without prior knowledge of the environment.

The design of Hydra consists of two main components.

First, we mathematically model diffuse multi-bounce scattering, which provides the basis for multi-bounce spatial domain matched filtering to localize beyond-FoV objects.

Second, we design a sequential detection and localization pipeline that (i) separately detects objects along single-, double- and triple-bounce paths, and (ii) then uses prior detections as anchors to localize objects using multi-bounce despite their weaker power. We note that no prior environment knowledge is assumed in any of the steps.

Hydra's overall algorithmic flow is depicted in Fig. 3.

4.1 Modeling Multi-Bounce Paths

We begin by extending (1) and (2) to model multi-bounce.

Consider *double-bounce* paths of the form: radar $\rightarrow \mathbf{p} \rightarrow \mathbf{p}' \rightarrow$ radar, for pairs of locations $\mathbf{p} \neq \mathbf{p}' \in \mathbb{R}^2$ in the environment, as illustrated in Fig. 4(a). The angles-of-departure and arrival are different for such paths, i.e., $\theta^{\ell}_{\text{TX}} \neq \theta^{\ell}_{\text{RX}}$, and given by $\theta^{\ell}_{\text{TX}} = \theta_{\mathbf{p}}$, $\theta^{\ell}_{\text{RX}} = \theta_{\mathbf{p}'}$. The time delay is the combined delay of the path through $\mathbf{p}$ & $\mathbf{p}'$, i.e., $\tau_{\ell} = \frac{\text{d}_{\mathbf{p};\mathbf{p}'}}{\text{c}}$, where $\text{d}_{\mathbf{p};\mathbf{p}'} = \|\mathbf{p}\|_2 + \|\mathbf{p} - \mathbf{p}'\|_2 + \|\mathbf{p}'\|_2$. Furthermore, the path attenuation can be modeled as the combined reflectivity and path loss of the path through $\mathbf{p}$ & $\mathbf{p}'$, $\alpha_{\ell} = \sigma_{\mathbf{p};\mathbf{p}'}$. Hence, the double-bounce system model is

$$\mathbf{y}_{\text{DB}}(t) = \sum_{\substack{\mathbf{p},\mathbf{p}' \\ \mathbf{p}' \neq \mathbf{p}}} \sigma_{\mathbf{p};\mathbf{p}'} \mathbf{a}_{\text{RX}}(\theta_{\mathbf{p}'}) \mathbf{a}^{\top}_{\text{TX}}(\theta_{\mathbf{p}}) \mathbf{w}_{\text{TX}} x\left(t - \frac{\text{d}_{\mathbf{p};\mathbf{p}'}}{\text{c}}\right). \quad (7)$$

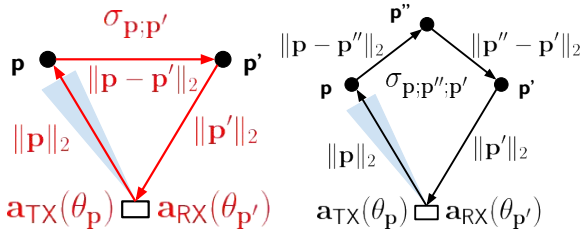

(a) Double-bounce paths **(b) Triple-bounce paths**

Figure 4: Modeling double- and triple-bounce paths.

Note that valid locations of points $\mathbf{p}'$ in the above equation and Fig. 4(a) are limited to locations *in front* of the radar, for the radar to be able to capture reflections from $\mathbf{p}'$.

Next, consider *triple-bounce* paths of the form: radar $\rightarrow \mathbf{p} \rightarrow \mathbf{p}'' \rightarrow \mathbf{p}' \rightarrow$ radar, for triplets of locations $\mathbf{p} \neq \mathbf{p}'' \neq \mathbf{p}' \in \mathbb{R}^2$ in the environment, as illustrated in Fig. 4(b). Note that we have not enforced any relationship between $\mathbf{p}$ & $\mathbf{p}'$ to include the special case $\mathbf{p} = \mathbf{p}'$, when triple-bounce occurs between only two locations. The angles-of-departure and arrival are given by $\theta^{\ell}_{\text{TX}} = \theta_{\mathbf{p}}$, $\theta^{\ell}_{\text{RX}} = \theta_{\mathbf{p}'}$. The time delay is the combined delay of the path through $\mathbf{p}$, $\mathbf{p}''$ & $\mathbf{p}'$, i.e., $\tau_{\ell} = \frac{\text{d}_{\mathbf{p};\mathbf{p}'';\mathbf{p}'}}{\text{c}}$, where $\text{d}_{\mathbf{p};\mathbf{p}'';\mathbf{p}'} = \|\mathbf{p}\|_2 + \|\mathbf{p} - \mathbf{p}''\|_2 + \|\mathbf{p}'' - \mathbf{p}'\|_2 + \|\mathbf{p}'\|_2$. The path attenuation is the combined reflectivity and path loss of the path through $\mathbf{p}$, $\mathbf{p}''$ & $\mathbf{p}'$, $\alpha_{\ell} = \sigma_{\mathbf{p};\mathbf{p}'';\mathbf{p}'}$. Hence, the triple-bounce system model is

$$\mathbf{y}_{\text{TB}}(t) = \sum_{\substack{\mathbf{p},\mathbf{p}',\mathbf{p}'' \\ \mathbf{p} \neq \mathbf{p}'' \neq \mathbf{p}'}} \sigma_{\mathbf{p};\mathbf{p}'';\mathbf{p}'} \mathbf{a}_{\text{RX}}(\theta_{\mathbf{p}'}) \mathbf{a}^{\top}_{\text{TX}}(\theta_{\mathbf{p}}) \mathbf{w}_{\text{TX}} x\left(t - \frac{\text{d}_{\mathbf{p};\mathbf{p}'';\mathbf{p}'}}{\text{c}}\right). \quad (8)$$

We note that valid locations of points $\mathbf{p}''$ in the above equation and Fig. 4(b) are not only limited to locations in front of the radar, but can also include locations *behind the radar*, as long as locations $\mathbf{p}'$ are in front of the radar.

Arbitrary nth-bounce can be modeled similarly:

$$\mathbf{y}_{\text{n-B}}(t) = \sum_{\substack{\mathbf{p}_1,\cdots,\mathbf{p}_n \\ \mathbf{p}_1 \neq \cdots \neq \mathbf{p}_n}} \sigma_{\mathbf{p}_{1\cdots n}} \mathbf{a}_{\text{RX}}(\theta_{\mathbf{p}_n}) \mathbf{a}^{\top}_{\text{TX}}(\theta_{\mathbf{p}_1}) \mathbf{w}_{\text{TX}} x\left(t - \frac{\text{d}_{\mathbf{p}_{1\cdots n}}}{\text{c}}\right),$$

where $\sigma_{\mathbf{p}_{1\cdots n}}$ and $\text{d}_{\mathbf{p}_{1\cdots n}}$ denote the combined reflectivity and path length of nth-bounce through locations $\mathbf{p}_1, \cdots, \mathbf{p}_n$. The overall system model in (1) is then the sum of all multi-bounce components, $\mathbf{y}(t) = \mathbf{y}_{\text{SB}}(t) + \mathbf{y}_{\text{DB}}(t) + \mathbf{y}_{\text{TB}}(t) + \cdots$.

We note that the above model is valid only for *diffuse* multi-bounce scattering, which assumes that all objects in the environment scatter incoming waves *omni-directionally*. Our primary motivation for using a diffuse scattering model is to meet our overall goal of sensing *without* requiring any prior knowledge of the material properties of the environment. Despite its limitations, our model and subsequent approach yield good performance across a wide variety of specular and diffuse objects, as detailed in our evaluation (Section 5).

4.2 Multi-Bounce Spatial Matched Filtering

4.2.1 Motivation: Multipath "Ghosts". We first motivate the need for developing a multi-bounce matched filtering method. Consider two point objects at ranges X and Y, and azimuth angles ϕ and $-\theta$. For simplicity, assume an occluded direct path to Object 2; hence, the radar receives signals along single-bounce (radar $\rightarrow$ Object1 $\rightarrow$ radar) and triple-bounce (radar $\rightarrow$ Object1 $\rightarrow$ Object2 $\rightarrow$ Object1 $\rightarrow$ radar) paths:

$$\mathbf{y}(t) = \sigma_1 \mathbf{a}_{\text{RX}}(\theta)\, \mathbf{a}_{\text{TX}}^{\top}(\theta)\, \mathbf{w}_{\text{TX}} \left[x\left(t - \frac{2\text{Y}}{\text{c}}\right) + \sigma_1\sigma_2 x\left(t - \frac{2\text{d}_{\text{TB}}}{\text{c}}\right)\right],$$

where $\text{d}_{\text{TB}} = \text{Y} + \sqrt{\text{X}^2 + \text{Y}^2 - 2\text{XY}\cos(\theta+\phi)}$ is the one-way length of the triple-bounce path. Directly applying the single-bounce matched filter from (4) yields two locations with high reflectivity values: (i) the actual target location at range Y and angle $-\theta$, and (ii) a "ghost" of Object 2 about Object 1, at range d_{TB} and angle $-\theta$. Without prior knowledge about Object 1's location, it is challenging to differentiate between actual objects and "ghosts", and in case of the latter, remap them to their ground-truth locations. Therefore, we develop an approach to automatically localize objects sensed along multi-bounce paths to their ground-truth location, without "ghost" detection and remapping.

4.2.2 Proposed Approach. To avoid "ghost" remapping, we propose to directly estimate the multi-bounce reflectivities of objects via a multi-bounce extension of the single-bounce adjoint inversion (matched filtering) approach from (4).

Let $\tilde{\mathbf{y}}_{\text{DB}}(\omega), \tilde{\mathbf{y}}_{\text{TB}}(\omega), \cdots$ denote the multi-bounce system models from (7)-(8) in the frequency domain after matched filtering with transmit signal $x(t)$. In the case of double-bounce, we directly estimate the double-bounce reflectivity, $\sigma_{\mathbf{p};\mathbf{p}'}$, at location $\mathbf{p}'$ due to reflection from location $\mathbf{p}$ as

$$\hat{\sigma}_{\mathbf{p};\mathbf{p}'} = \frac{1}{\text{W}} \sum_{\omega} \left(\mathbf{a}_{\text{TX}}^{\top}(\theta_{\mathbf{p}})\mathbf{w}_{\text{TX}}\right)^{*} e^{j\omega\frac{\text{d}_{\mathbf{p};\mathbf{p}'}}{\text{c}}} \mathbf{a}_{\text{RX}}^{\text{H}}(\theta_{\mathbf{p}'})\tilde{\mathbf{y}}_{\text{DB}}(\omega). \quad (9)$$

Intuition: (9) may be understood as: *receive beamforming* to locations $\mathbf{p}'$ (via $\mathbf{a}_{\text{RX}}^{\text{H}}(\theta_{\mathbf{p}'})\tilde{\mathbf{y}}_{\text{SB}}(\omega)$), while *transmit beamforming* towards $\mathbf{p}$ and compensating for the double-bounce path length via $\mathbf{a}_{\text{TX}}^{\top}(\theta_{\mathbf{p}})\mathbf{w}_{\text{TX}} e^{-j\omega\frac{\text{d}_{\mathbf{p};\mathbf{p}'}}{\text{c}}}$. Since only the receive beamforming term depends on $\mathbf{p}'$, the angular resolution of (9) is limited to the angular resolution of the receive array, as also illustrated in Fig. 5(a). In contrast, virtual array formation due to same transmit and receive beamforming directions in single-bounce enable higher angular resolution.

In triple-bounce, we estimate the triple-bounce reflectivity, $\sigma_{\mathbf{p};\mathbf{p}'';\mathbf{p}'}$, at location $\mathbf{p}''$ due to reflections from locations $\mathbf{p}$, $\mathbf{p}'$,

$$\hat{\sigma}_{\mathbf{p};\mathbf{p}'';\mathbf{p}'} = \frac{1}{\text{W}} \sum_{\omega} \left(\mathbf{a}_{\text{TX}}^{\top}(\theta_{\mathbf{p}})\mathbf{w}_{\text{TX}}\right)^{*} e^{j\omega\frac{\text{d}_{\mathbf{p};\mathbf{p}'';\mathbf{p}'}}{\text{c}}} \mathbf{a}_{\text{RX}}^{\text{H}}(\theta_{\mathbf{p}'})\tilde{\mathbf{y}}_{\text{TB}}(\omega). \quad (10)$$

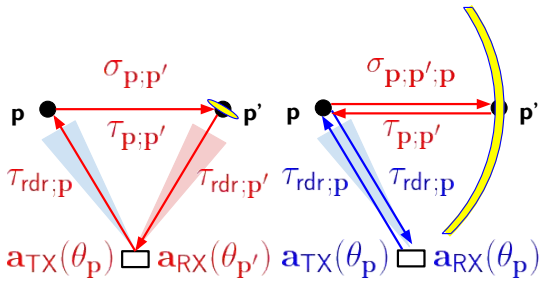

(a) Double-bounce **(b) Triple-bounce**

Figure 5: Intuitive understanding of double- and triple-bounce adjoint inversion (matched filtering) in (9)-(10).

Intuition: The dependence on the triple-bounce object $\mathbf{p}''$ is only in the *distance* term $\text{d}_{\mathbf{p};\mathbf{p}'';\mathbf{p}'}$. Hence, a single triple-bounce path from points $\mathbf{p}$, $\mathbf{p}'$, (10) can only result in an arc at point $\mathbf{p}''$, as shown in Fig. 5(b) for $\mathbf{p}' = \mathbf{p}$, $\mathbf{p}'' = \mathbf{p}'$. Reducing the uncertainty from an arc to a unique point requires at least three distinct triple-bounce paths passing through $\mathbf{p}''$.

Extensions to arbitrary nth-bounce follow similarly:

$$\hat{\sigma}_{\mathbf{p}_{1\cdots n}} = \frac{1}{\text{W}} \sum_{\omega} \left(\mathbf{a}_{\text{TX}}^{\top}(\theta_{\mathbf{p}_1})\mathbf{w}_{\text{TX}}\right)^{*} e^{j\omega\frac{\text{d}_{\mathbf{p}_{1\cdots n}}}{\text{c}}} \mathbf{a}_{\text{RX}}^{\text{H}}(\theta_{\mathbf{p}_n})\tilde{\mathbf{y}}_{\text{n-B}}(\omega).$$

In the next subsection, we demonstrate how the developed matched filtering approach is used to detect and localize beyond-FoV objects via multi-bounce.

4.3 Sequential Detection & Localization

Extending the matched filtering approach from Section 4.2 to solve the general problem of beyond-FoV target detection requires contending with two fundamental challenges: (i) the power of single-bounce greatly dominates over higher-order bounces, and (ii) lack of prior environment knowledge. To tackle these challenges, we propose a *sequential* detection and localization approach, wherein objects in the environment are first detected via single-bounce, then double-bounce, followed by triple-bounce, and so on. We describe our procedure sequentially, beginning with single-bounce. Throughout, we assume the transmit beamforming weights $\mathbf{w}_{\text{TX}}$ are fixed and known to the radar.

4.3.1 Stage 1: Single-Bounce. The procedure begins with single-bounce sensing. The radar first forms a spatial map of its surroundings $\{\hat{\sigma}_{\mathbf{p}}\}$ via the single-bounce adjoint inversion in (4). To detect key objects in the environment, we use 2D ordered statistics (OS) CFAR [35]. In brief, OS-CFAR computes the target-to-clutter ratio (TCR) corresponding to each location $\mathbf{p}$ in the environment, where the target power at $\mathbf{p}$ is defined as the reflectivity intensity, $|\hat{\sigma}_{\mathbf{p}}|^2$, and the clutter power is the median value of reflectivity intensities of points in a local neighborhood around $\mathbf{p}$. The computed TCR is then compared to a threshold, empirically chosen as 0.5×

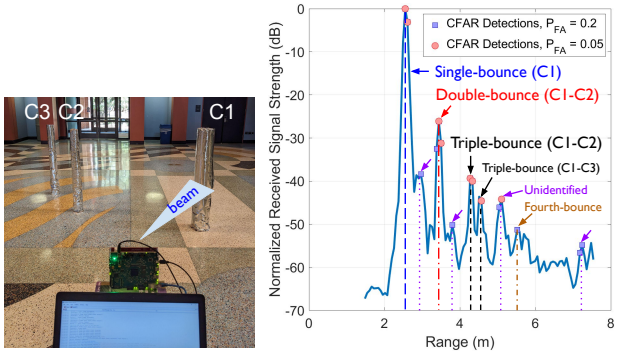

(a) Setup **(b) Range plot**

Figure 6: Fourth-bounce power too weak to be used.

the maximum TCR amongst all single-bounce reflectivities. The output corresponds to the set of objects detected via single-bounce. If an object is detected at a higher range but same angle as another detection, the higher range object is zeroed out since such a detection can only correspond to a "ghost" and not a physical object. We denote the final set of locations of single-bounce object detections by S_1.

4.3.2 Stage 2: Double-Bounce. Next, the radar uses double-bounce to localize beyond-FoV objects. For each single-bounce detected point $\mathbf{p} \in S_1$, the radar estimates the double-bounce reflectivity $\hat{\sigma}_{\mathbf{p};\mathbf{p}'}$ via (9) for locations $\mathbf{p}'$ in the environment. We ensure that locations $\mathbf{p}'$ do not coincide with detected single-bounce objects $\mathbf{p} \in S_1$ (for zero interference between bounces), and moreover lie outside the radar's transmit main-lobe. The double-bounce reflectivity magnitude of the individual point $\mathbf{p}'$ is found by averaging magnitudes of $\hat{\sigma}_{\mathbf{p};\mathbf{p}'}$ over all single-bounce detections $\mathbf{p} \in S_1$, $|\hat{\sigma}^{\text{DB}}_{\mathbf{p}'}| = \frac{1}{|S_1|}\sum_{\mathbf{p}\in S_1} |\hat{\sigma}_{\mathbf{p};\mathbf{p}'}|$. OS-CFAR is then used to update the set of double-bounce object detections S_2, with threshold $0.5\times$ the maximum TCR of all double-bounce reflectivities.

4.3.3 Stage 3: Triple-Bounce. The above procedure is then repeated for higher-order multi-bounce orders. For triple-bounce, $\hat{\sigma}_{\mathbf{p};\mathbf{p}'';\mathbf{p}'}$ is estimated via (10) for each single- and double-bounce pair $(\mathbf{p}, \mathbf{p}') \in S_1 \times S_2$, for locations $\mathbf{p}'' \notin S_1 \cup S_2$. Triple-bounce reflectivity magnitudes of points $\mathbf{p}''$ are found via averaging, $|\hat{\sigma}^{\text{TB}}_{\mathbf{p}''}| = \frac{1}{|S_1 \times S_2|}\sum_{(\mathbf{p},\mathbf{p}')\in S_1\times S_2} |\hat{\sigma}_{\mathbf{p};\mathbf{p}'';\mathbf{p}'}|$, and OS-CFAR is used to update the triple-bounce set S_3 as before. The procedure can be similarly extended to nth-bounce.

4.3.4 Stopping Criteria. While the above procedure can be performed up to arbitrary multi-bounce orders n, empirically we observe that the received power of fourth- and higher-order bounces is too low to be exploited. Fig. 6(b) plots the range profile (power normalized to single-bounce path) for a toy experiment conducted with three metallic cylinders, with the radar transmitting towards C1, and C2 occluding C3 outside the transmit beam. We observe that the power of fourth-bounce paths (e.g., radar → C1 → C3 → C1 → C2 → radar) is much weaker than triple-bounce, with peaks buried within the clutter and noise levels. Hence, in our evaluation, we do not process beyond triple-bounce.

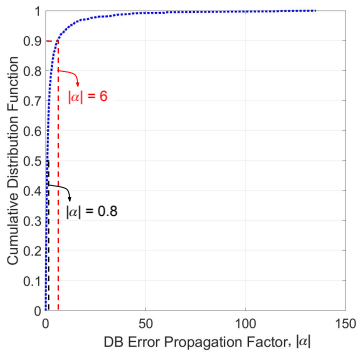

Figure 7: Error propagation analysis (Lemma 4.1).

4.3.5 Computational Complexity. The computational complexity of each adjoint inversion step, e.g., (4), (9) or (10), is $O(\text{TRW})$, where T/R is the number of transmit/receive elements and W is the number of considered frequencies. Hence, in single-bounce, for P locations $\mathbf{p}$ over which (4) is evaluated, the total complexity is $O(\text{TRWP})$. The target detection steps (OS-CFAR and thresholding) are also $O(\text{P})$; hence the total complexity of single-bounce is $O(\text{TRWP})$. Given $|S_1|$ single-bounce detections, the complexity of running the double-bounce adjoint inversion step (9) over $|S_1|$ locations $\mathbf{p}$ and P locations $\mathbf{p}'$ is $O(\text{TRW}|S_1|\text{P})$. Analogously, the complexity of triple-bounce via (10) is $O(\text{TRW}|S_1 \times S_2|\text{P})$. In our evaluation, $|S_n| \leq 6$, $\forall n \in \{1, 2\}$, and each iteration takes 11.98 s on average (with 0.25 s standard deviation) for our MATLAB Intel i5 CPU-based implementation (which can be further optimized via GPU implementation).

4.3.6 Error Propagation. Given the iterative nature of our algorithm, one may expect errors in previous iterations to propagate into the current iteration. To quantify potential error propagation, we study the simple double-bounce configuration depicted in Fig. 4(a) with two point objects at $\mathbf{p}$ and $\mathbf{p}'$, and quantify the error in localizing $\mathbf{p}'$ as a function of the error in localizing $\mathbf{p}$.

LEMMA 4.1. *Let $\Delta_{\text{SB}} = \hat{\mathbf{p}} - \mathbf{p}$ be the location error vector for localizing $\mathbf{p}$ via single-bounce adjoint inversion in* (4)*. Then, the location error vector $\Delta_{\text{DB}} = \hat{\mathbf{p}}' - \mathbf{p}'$ for localizing $\mathbf{p}'$ via double-bounce adjoint inversion in* (9) *is given by:*

$$\Delta_{\text{DB}} = \alpha\Delta_{\text{SB}} = \frac{\left\langle \Delta_{\text{SB}}, \frac{\mathbf{p}-\mathbf{p}'}{\|\mathbf{p}-\mathbf{p}'\|_2} + \frac{\mathbf{p}}{\|\mathbf{p}\|_2} \right\rangle}{\left\langle \Delta_{\text{SB}}, \frac{\mathbf{p}-\mathbf{p}'}{\|\mathbf{p}-\mathbf{p}'\|_2} - \frac{\mathbf{p}'}{\|\mathbf{p}'\|_2} \right\rangle}\Delta_{\text{SB}}.$$

The above result is proved in Appendix B. Fig. 7 plots the cumulative distribution function (CDF) of the magnitude of

(a) S1 (b) S2 (c) S3 (d) S4 (e) S5

Figure 8: Indoor & outdoor experiment scenarios.

the scaling factor $|\alpha|$ relating $\mathbf{\Delta}_{\text{DB}}$ and $\mathbf{\Delta}_{\text{SB}}$ over 1000 independent trials with randomly generated locations $\mathbf{p} \neq \mathbf{p}'$. The median value of $|\alpha|$ is 0.8 and its 90th-percentile value is 6; hence the impact of single-bounce localization error on double-bounce error would be at most 6× (with 90% probability). Hence, lower error in single-bounce localization will yield lower localization errors in double-bounce with Hydra.

4.3.7 Compatibility with Beam Steering. The proposed procedure can be easily extended to a beam steering radar. Given a set of transmit beamforming weights $\mathbf{w}_{\text{TX}} \in \mathbf{W}_{\text{TX}}$, the procedure in each of the above stages can be performed for each $\mathbf{w}_{\text{TX}} \in \mathbf{W}_{\text{TX}}$ to yield an object detection set $\mathbf{S}_n(\mathbf{w}_{\text{TX}})$. Subsequently, the union of sets $\mathbf{S}_n = \cup_{\mathbf{W}_{\text{TX}}} \mathbf{S}_n(\mathbf{w}_{\text{TX}})$ can be passed to the $(n+1)$th stage of our procedure.

5 PERFORMANCE EVALUATION

5.1 Implementation & Methodology

Implementation: We implement Hydra on a commercial digital mmWave MIMO radar, AWR2243 cascade radar [18] from Texas Instruments, which supports up to 12 transmit and 16 receive elements and operates in the 76 − 81 GHz band. We only use 9 of the 12 total transmit elements since we only sense in azimuth and not elevation. We configure the radar to transmit beamforming mode; each transmission consists of 10 frames[3] with 64 FMCW chirps of duration 40μs and slope 79 MHz/μs per frame. A laptop with Intel i5 CPU and 12 GB RAM is used to control the radar and process data. All processing is performed via custom MATLAB functions. In our results, we discretize the range-azimuth plane into 6 cm × 1° resolution bins. We use a 2D OS-CFAR detector with a sliding window of size 17×17 bins, with the cell-under-test and guard window occupying the middle 7 × 7 bins.

Experiment Scenarios: We collect data in five indoor and outdoor scenarios (Fig. 8) - a large indoor hall (S1), an indoor lobby (S2), an indoor U-shaped staircase bend (S3), an outdoor building corridor (S4), and an outdoor terrace (S5). In all cases, the radar is at a height of 1 m above the ground.

Data Collection: We configure the radar to transmit in an experiment-specific azimuth angle set $\Theta \subseteq [-60°, +60°]$ and capture reflections from the surrounding environment in the presence of different objects (room furniture, humans[4], etc.). We ensure the radar and the environment remain static during our experiments; mobility is left for future work.

Ground Truth: We establish ground truth object locations in the environment with respect to the radar via measurements with a measuring tape and laser distance range finder.

Baseline: We compare Hydra with single-bounce sensing via (4) utilizing both main- and side-lobes of the radar's transmit beampattern, and also proposed in [48]. We note that our choice of baseline is equivalent to methods that identify and suppress multipath "ghosts" observed at the output of single-bounce processing [6, 10, 21]. In contrast, Hydra incorporates multi-bounce into the radar signal processing pipeline and does not require explicit "ghost" identification.

Performance Metrics: We evaluate the overall performance of Hydra via the localization error for a beyond-FoV human. Since the output of Hydra is generally a collection of points, we define the localization error as the minimum distance between the human's ground truth location and the set of locations outputted by Hydra. We also use the received signal strength (RSS) along multi-bounce paths, with appropriate normalization, in our microbenchmark evaluation.

5.2 Qualitative System Demonstration

First, we demonstrate double-bounce sensing of humans *outside the radar's transmit beam*. Fig. 9(a) shows the experiment setup in Scenario S1 with two humans, Human 1 (H1) at 2.5 m, −15° and Human 2 (H2) at 2.5 m, +30°. Figs. 9(b)-(c) show the single-bounce and double-bounce target-to-clutter ratio (TCR) maps outputted by Hydra. We observe that H2 is not detected in the single-bounce output (Fig. 9(b)), because its TCR is below the single-bounce detection threshold. However, with appropriate double-bounce processing, H2 is detected near its ground-truth location in Fig. 9(c), albeit with lower TCR as compared to the single-bounce detection of H1. We further present double-bounce outputs for different choices of reflectors in place of H1 - a whiteboard in Fig. 9(d) and a brick pillar in Fig. 9(e). Besides localizing the human near its ground-truth location, we also observe that the double-bounce TCR is material dependent - lowest for brick pillar (21 dB), followed by whiteboard (25 dB) and human (26 dB). We exhaustively quantify the impact of reflector material on performance later in Section 5.4.

Next, we demonstrate sensing *around-corners* and *behind-the-radar* using triple-bounce. Fig. 10(a) shows the around-corner experiment setup in Scenario S3, with a radar and human on opposite ends of the U-shaped staircase bend. The radar transmits in $[-30°, 30°]$ to capture multiple points on the staircase bend via single-bounce, which are subsequently

[3] we average data across frames to boost received signal-to-noise ratio

[4] all our experiments involving human subjects have been performed with Institutional Review Board (IRB) approval

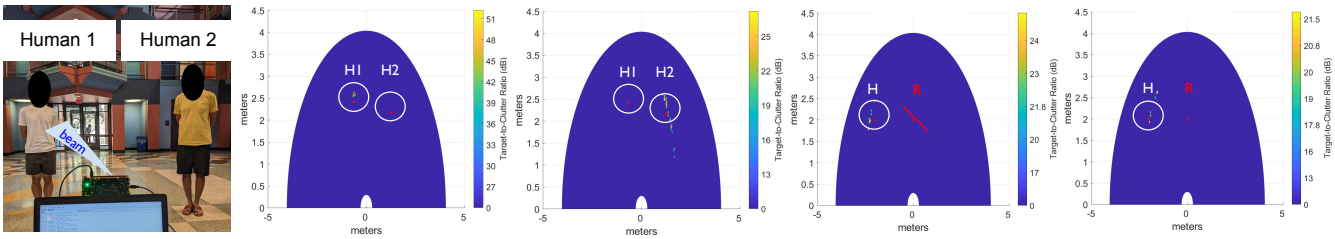

(a) Setup in S1 (b) Single-bounce (c) Double-bounce (d) Whiteboard (S2) (e) Brick pillar (S4)

Figure 9: Double-bounce sensing of a human standing outside the radar's transmit beam. (a): Setup in S1, with radar configured to transmit towards Human 1 (H1). (b)-(c): H1 detected via single-bounce, H2 detected via double-bounce. (d)-(e): Double-bounce outputs for similar setup as in (a) but with whiteboard and brick pillar in place of Human 1.

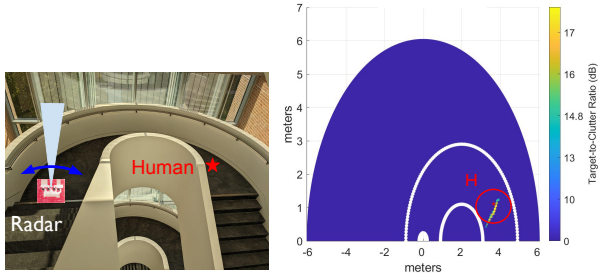

(a) Setup in S3 (b) Triple-bounce output

Figure 10: Triple-bounce around-corner sensing of a human standing on the opposite end of a U-shaped staircase bend, with radar transmitting in $[-30°, 30°]$.

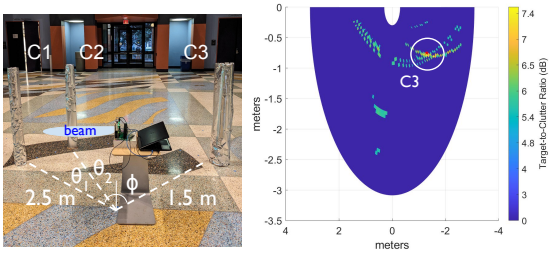

(a) Setup in S1 (b) Triple-bounce output

Figure 11: Triple-bounce behind-radar sensing of a metallic cylinder C3 at $\phi = 30°$, with radar transmit beamforming to C1 at $\theta_1 = 75°$, and C2 kept at $\theta_2 = 30°$.

used to localize the beyond-FoV human via triple-bounce. We ensure triple-bounce from only the human and not the staircase via background subtraction, i.e., capturing two measurements - one with the human and the other without - and subtracting the two to remove intra-staircase multi-bounce. Fig. 10(b) shows successful human localization in this case.

Finally, Fig. 11(a) shows the behind-radar experiment setup in Scenario S1, with a radar transmitting towards a metallic cylinder C1, aiming to localize C2 outside the transmit beam via double-bounce and C3 behind the radar via triple-bounce.

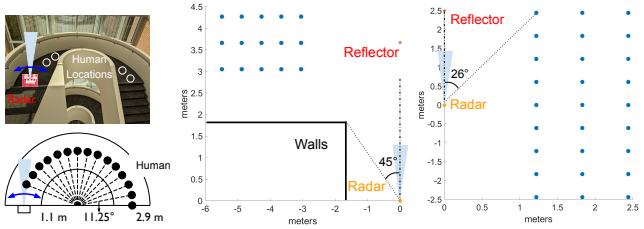

(a) Setup 1 (S3) (b) Setup 2 (S5) (c) Setup 3 (S2)

Figure 12: Experiment setups to evaluate overall localization error of Hydra for a human target standing in various grid locations marked with filled black/blue circles. The radar transmit beamforms towards $[-30°, 30°]$ in (a), and towards the reflectors at $0°$ in (b) and (c).

Since only C1 is illuminated directly, there are only two possible triple-bounce paths: radar → C1 → C3 → C1 → radar and radar → C1 → C3 → C2 → radar. Fig. 11(a) shows the triple-bounce output of Hydra, showing two arcs corresponding to the triple-bounce paths intersecting with maximum TCR at the ground-truth location of C3. Fig. 11(b) is significantly "noisier" and has lower TCRs compared to Fig. 10(b) due to lower number of paths (2) to average over in Stage 3 of Hydra's processing (Section 4.3.3).

5.3 Overall System Performance

We quantify the overall system performance via exhaustive human localization experiments in Scenarios S2, S3 and S5. In each experiment, a human stands in different locations on a 2D grid, as shown in Figs. 12(a)-(c). Figs. 12(a)-(b) correspond to around-corner scenarios, where the radar uses reflections from either the U-shaped staircase bend in Fig. 12(a) or a small reflector (metal trashcan) in Fig. 12(b) to localize the human. The grid in Fig. 12(c) includes locations in front of and behind the radar, and the radar uses reflections from the reflector (metal trashcan) to localize the human.

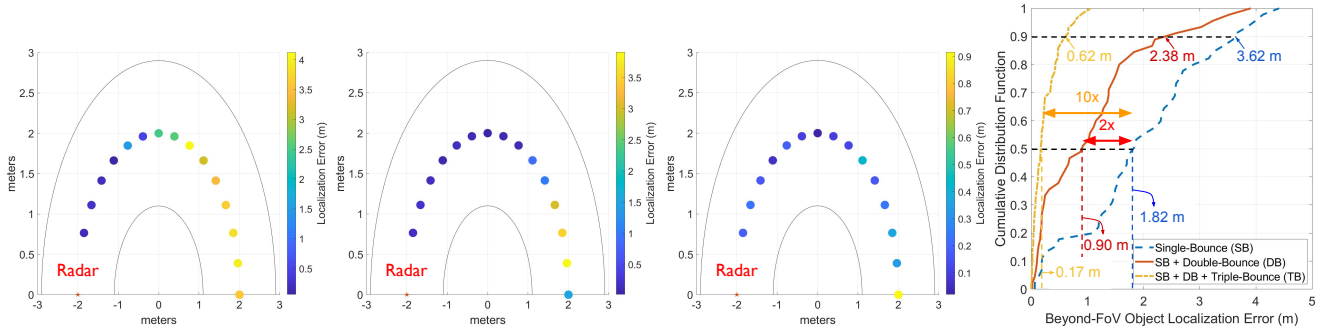

(a) Single-bounce (SB) (b) SB + Double-bounce (DB) (c) SB + DB + Triple-bounce (d) Overall loc. error CDF

Figure 13: Overall system performance. (a)-(c): Human localization error for setup in Fig. 12(a) across different grid locations. As higher orders of multi-bounce are exploited, the human is localized with sub-0.5 m error in more grid locations. (d): Statistics of human localization error across Setups 1-3 from Fig. 12. Adding double-bounce and triple-bounce decreases the median localization error by 2× and 10× respectively as compared to single-bounce.

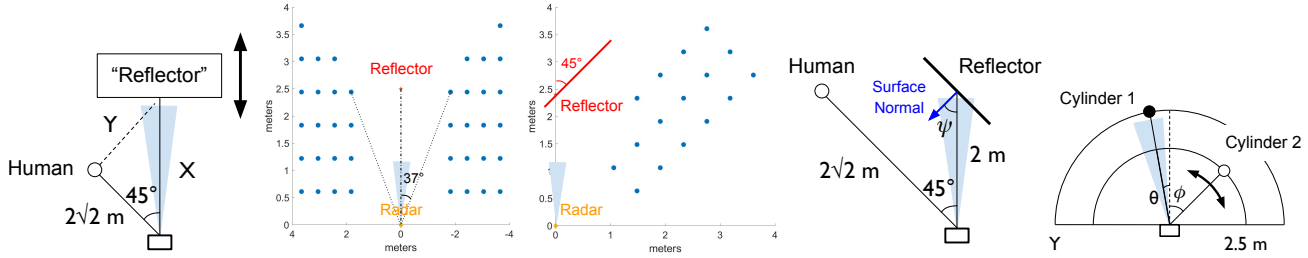

(a) Setup 4 (S2) (b) Setup 5 (S2) (c) Setup 6 (S2) (d) Setup 7 (S2) (e) Setup 8 (S1)

Figure 14: Experiment setups for single-reflector microbenchmark evaluation of Hydra's beyond-FoV localization.

Figs. 13(a)-(c) visualize the localization error across different human locations in Setup 1 from Fig. 12(a). As higher orders of multi-bounce beyond single-bounce are exploited, the human is localized with sub-0.5 m error in more grid locations; effectively increasing the sensing FoV of the radar.

Fig. 13(d) shows the overall statistics of the beyond-FoV human localization errors across all three setups from Fig. 12. Compared to single-bounce only processing, the median error decreases by 2× on adding double-bounce, and by 10× on further adding triple-bounce. We observe similar 1.5×-5× reduction in the 90th-percentile errors on adding double- and triple-bounce, showing the benefit of using multi-bounce.

Note that the ground-truth locations used in our localization error calculations are based on the 2D grid locations where a human stands. Given that human bodies have finite diameters, in practice, reflections may occur from a slightly offset point on the body compared to its centroid, explaining why our best median errors are in the order of $0.1 - 0.2$ m.

5.4 Microbenchmark Evaluation

Finally, we evaluate the impact of various system parameters on the beyond-FoV human localization performance. For ease of evaluation, we only process up to double-bounce. Throughout our evaluation, we label the objects within the radar's transmit beam as "reflectors".

Impact of Reflector Material: We begin by quantifying the impact of the material properties of a single reflector placed within the radar's transmit beam. We perform exhaustive experiments in three different configurations shown in Figs. 14(a)-(c) for different reflector choices. In Fig. 14(a), the radar transmits towards a reflector at 0° while the human stands still at range $2\sqrt{2}$ m and angle $-45°$ from the radar. Three different reflectors (metal trashcan, another human and a plastic chair) are moved from range X = 1.22 m to X = 6.1 m in steps of 0.61 m. Note that the double-bounce range as per Fig. 14(a) is $d_{DB} = 0.5(X + Y + 2\sqrt{2})$ m. As our first evaluation metric, we use the double-bounce RSS, which is normalized by the single-bounce RSS for a human standing at a single-bounce range of d_{DB} in order to cancel out the distance dependence and only retain the impact of

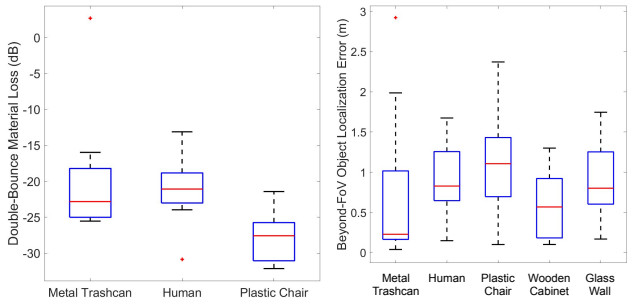

(a) RSS vs material **(b) Loc. error vs material**

Figure 15: Impact of reflector material on double-bounce RSS and localization error (microbenchmark).

reflector material. Fig. 15(a) shows that the RSS of the metal trashcan and human is roughly similar, with median values of −23 dB and −22 dB respectively. However, the RSS of the plastic chair is much lower than both, with median value −27 dB. Therefore, we expect better system performance with highly reflective objects, such as metals or human bodies, as compared to lower reflectivity objects made of plastic.

Next, we quantify the impact of the reflector material on the overall localization error for the setups in Figs. 14(b)-(c). In Fig. 14(b), the radar transmits towards different small reflectors (metal trashcan, another human and plastic chair) kept fixed at range 2.5 m and 0°, while the human stands at different locations on the marked 2D grid. In Fig. 14(c), the radar transmit beam sweeps from $[-30°, 30°]$ to sample different points on different extended reflectors (wooden cabinet and glass wall), while the human stands at different locations on the marked 2D grid. Fig. 15(b) plots the localization error statistics for different materials. As expected from our conclusion from Fig. 15(a), we observe that the median localization error is lowest for the metal trashcan, followed by that of the human (with similar variance), and then the plastic chair (largest median error and variance). However, counter-intuitively, the wooden cabinet has lower localization error than the glass wall. We believe the high reflectivity of glass and metallic features on the wall degrade `Hydra`'s localization performance. However, exploiting multiple double-bounce paths from different points on the surface of extended reflectors reduces the localization error variance as compared to small reflectors.

Impact of Range: To quantify the impact of range, we consider the variation of the double-bounce RSS as a function of the double-bounce range $d_{DB} = 0.5(X + Y + 2\sqrt{2})$ m in the setup in Fig. 14(a). As per the well-known radar range equation, we expect the double-bounce RSS to vary as follows:

$$P_{RX,DB} = \frac{\alpha \sigma_{SB} \sigma_{DB}}{d_{DB}^4},$$

where α is a constant term collecting the effect of transmit and receive array gain, wavelength dependence, etc., and σ_{SB} and σ_{DB} are material-dependent reflectivities of the single-bounce reflector and double-bounce human. In Fig. 16(a), we plot the double-bounce RSS, with appropriate normalization to cancel out the constant α and material-dependent terms σ_{SB}, σ_{DB} (by using the mean material loss values obtained from Fig. 15(a)). We observe that the overall trend of the double-bounce RSS across all three considered materials matches theory (d_{DB}^{-4}) quite well. The discrepancies at close-by reflector ranges X = 1.22 m and X = 1.83 m for the metal trashcan possibly stem from the non-point object behavior of the trashcan at these distances, i.e., a larger portion of its surface contributes to double-bounce, boosting the RSS.

Impact of Reflector Orientation: We also quantify the dependence on reflector orientation by considering the double-bounce RSS as a function of the orientation angle ψ of the reflector's surface normal, for the setup shown in Fig. 14(d). We consider three reflectors: human body, whiteboard and plywood board. Fig. 16(b) shows that human body and plywood act as diffuse reflectors, scattering incoming signals omnidirectionally regardless of orientation. On the other hand, the whiteboard is strongly specular, with maximum RSS at $\psi = 45°$ - the optimal orientation for double-bounce reflections towards the human according to the law of reflection. We also observe a second-largest peak at $\psi = 90°$ due to reflections from the whiteboard's metallic edges that become oriented towards the radar at this angle.

Impact of Transmit Beam Direction: We further evaluate the impact of the radar's transmit beam direction on subsequent localization performance. We consider the setup shown in Fig. 14(e) with two metallic cylinders; the radar transmits towards Cylinder 1 at range Y m and angle θ, whereas Cylinder 2 is kept at different angles $\phi \in [-80°, 80°]$, in steps of 10°. We consider three different locations of Cylinder 1 - (Y = 3.5 m, $\theta = -10°$), (Y = 2.5 m, $\theta = 0°$), and (Y = 1.5 m, $\theta = 20°$). Fig. 16(c) shows that the localization error statistics for the three cases are similar, implying similar performance regardless of transmit beam direction. However, we note that the localization error variance is largest when (Y = 2.5 m, $\theta = 0°$) and smallest when (Y = 3.5 m, $\theta = -10°$). We explain this result on the basis of the transmit beampattern matrices from Fig. 2, where the beampattern has only two side-lobes within $\phi \in [-80°, 80°]$ when $\theta = 0°$, but four side-lobes otherwise. Thus, we expect single-bounce to be useful slightly less often when $\theta = 0°$ than otherwise, explaining the result. Moreover, (Y = 3.5 m, $\theta = -10°$) seems to perform best because the metallic cylinders are not exactly point objects; hence we expect the Cylinder 1 to scatter more energy towards Cylinder 2 when placed behind the latter.

Impact of Multiple Reflectors: Next, we evaluate the impact of exploiting double-bounce from multiple reflectors.

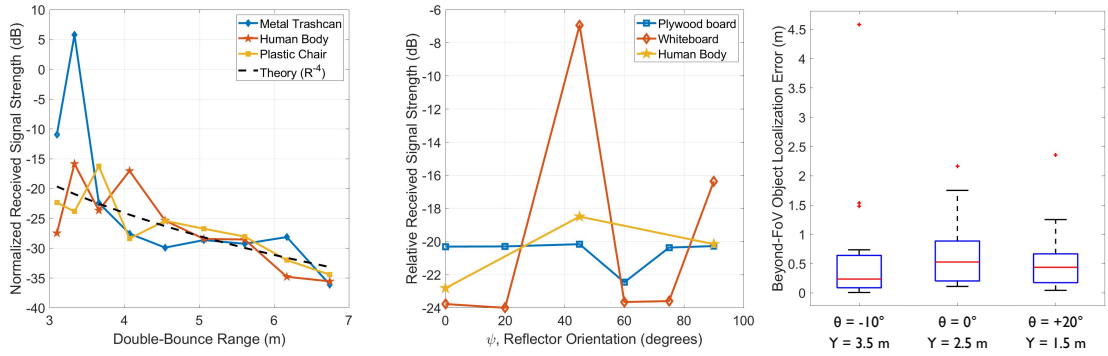

(a) RSS vs range **(b) RSS vs orientation** **(c) Loc. error vs TX direction**

Figure 16: Single-reflector microbenchmarks. (a) RSS decays as R^{-4} with double-bounce range. (b) RSS of whiteboard depends on orientation, but not of human or plywood. (c) Transmit beam direction does not impact performance.

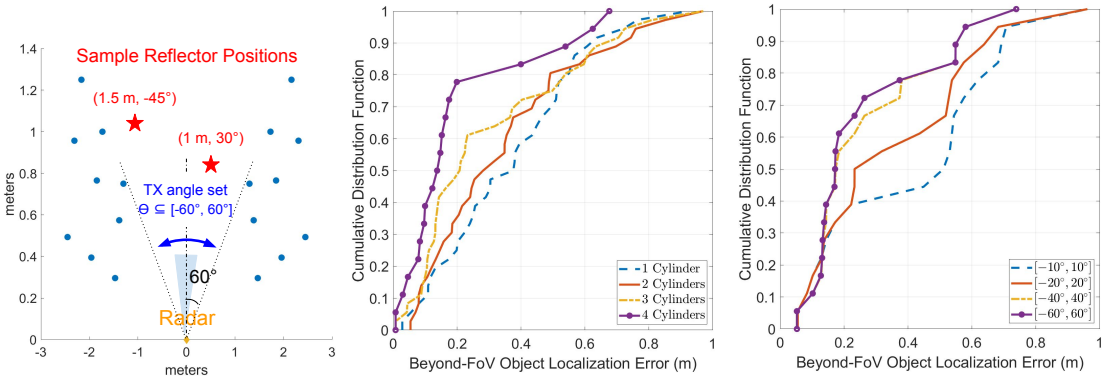

(a) Setup 9 (S2) **(b) Loc. error vs # reflectors** **(c) Loc. error vs TX angle set Θ**

Figure 17: Multi-reflector microbenchmarks. (a) Setup with multiple metallic cylinders (reflectors) in $[-60°, +60°]$. (b)-(c) Localization error improves with more number of reflectors and as a larger set $\Theta \subseteq [-60°, +60°]$ is illuminated.

We place multiple metallic cylinders (reflectors) and quantify the localization error statistics for a human standing on a grid of 18 locations outside $[-60°, 60°]$, as shown in Fig. 17(a). We configure the radar to beam sweep in $\Theta = [-40°, 40°]$ and place an increasing number of reflectors in $[-40°, 40°]$ at various locations in {(2 m, 0°), (1 m, 30°), (2 m, 30°), (2 m, −15°), (3 m, −15°), (2 m, 15°)}. Fig. 17(b) shows the CDF of localization errors across multiple scenarios with 1 to 4 reflectors. Overall, we observe that Hydra's performance improves as a higher number of reflectors are illuminated.

Impact of Radar Beam Sweep: Finally, we evaluate the impact of the beam sweep interval $\Theta \subseteq [-60°, 60°]$. We place 4 reflectors at locations (2 m, 0°), (2 m, 30°), (2 m, −15°), (2 m, −45°) and configure the radar to beam sweep in different sets $\Theta \in \{[-10°, 10°], [-20°, 20°], [-40°, 40°, [-60°, 60°]]\}$, such that different subsets of those 4 reflectors are illuminated. Fig. 17(c) shows that the CDF of localization errors improves with larger sets Θ, i.e., as more reflectors are illuminated.

6 DISCUSSION & LIMITATIONS

Multiple beyond-FoV & occluded targets: While we have evaluated Hydra's performance for single target (human) localization, in practice one may want to jointly localize multiple beyond-FoV targets, some of which may be occluded by other targets. Fig. 18 shows the double-bounce outputs corresponding to two possible multi-target scenarios. Hydra can localize two targets via double-bounce on opposite sides (Fig. 18(a)) or the same side (Fig. 18(b)) of a reflector, provided the targets do not occlude one another and are separated by $\geq 20°$. However, Hydra cannot localize objects occluded by other objects, e.g., H4 in Fig. 18(a), using double- and triple-bounce, and experimentally we did not observe significant fourth-bounce to use for such purposes. Future extensions to 3D object imaging could overcome this limitation.

Non-detections in single-bounce: A drawback of Hydra's sequential processing is that it relies on single-bounce detections in order to exploit further multi-bounce. Without

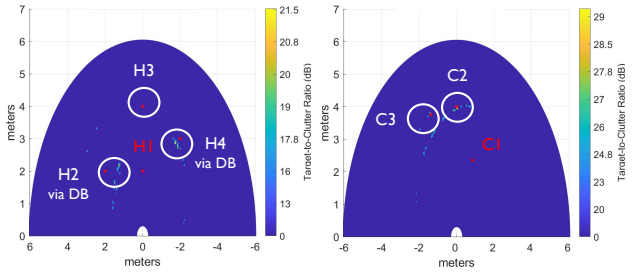

(a) Opposite sides of H1 **(b) Same side of C1**

Figure 18: Multiple beyond-FoV & occluded targets. (a) When radar transmits towards H1, H2 and H4 on opposite sides of H1 are detectable through double-bounce, but not H3 (occluded by H1). (b) When radar transmits towards C1, double-bounce detects C2 and C3 (separated by 20°), with a "target masking" effect on C3.

sufficient single-bounce detections on the reflector surface, e.g., when a small planar surface is oriented away from the radar, Hydra performs slightly worse than methods with perfect reflector knowledge [2, 44]. Table 2 shows the average localization errors in the around-corner setup from Fig. 12(b), for three different planar reflectors of length 0.5 m at a range of 3 m. Only center points on the reflectors are detected by Hydra, hence Hydra is outperformed by [2, 44].

Diffuse modeling: We assumed a diffuse model in Hydra to enable beyond-FoV sensing without prior environment knowledge. Future work will explore incorporating limited additional prior knowledge of the environment, e.g., material properties and surface normals, for finer-grained modeling.

Single-chip radars: We evaluated Hydra using a four-chip cascade MIMO radar [18] with 9 transmit and 16 receive elements (in azimuth). While the main concepts and modeling remain applicable to even single-chip radars, e.g., TI's AWR1843BOOST [17], adapting Hydra to such radars would require developing super-resolution routines in order to overcome their poorer azimuth resolution (∼ 15°).

Imaging extended objects: Although our evaluation in this paper is largely limited to localizing objects, we believe our techniques can also be adapted for imaging extended objects.

3D sensing with mobility: Hydra is limited to 2D range-azimuth sensing of static objects. Future work will also explore extensions to 3D sensing of mobile beyond-FoV objects.

Optimal reflector design: Finally, building upon Hydra which exploits natural multi-bounce in the environment, an interesting avenue for future work is the design of optimal reflectors, e.g., using metasurfaces, for beyond-FoV sensing.

7 CONCLUSION

In this paper, we described the design and evaluation of Hydra, a framework that uses multi-bounce scattering to enable beyond-field-of-view sensing with a single mmWave radar without prior knowledge of the environment. Our implementation on a commercial MIMO radar demonstrated the possibility of localizing humans outside the transmit beam, behind-the-radar and around-corners, with 2×-10× improvement in the median localization error in real-world scenarios even with no prior knowledge of the environment.

Method	Plywood board	Metal board	Whiteboard
Known refl.	0.24 m	0.16 m	0.11 m
Hydra	0.34 m	0.24 m	0.25 m

Table 2: Hydra has larger localization errors compared to methods with perfect reflector knowledge when the entire reflector surface is not mapped in single-bounce.

ACKNOWLEDGMENTS

We thank the anonymous reviewers and shepherd for their valuable suggestions. This work was supported in part by the National Science Foundation grants CAREER-1942902, CNS-1956297, CNS-2106921, CNS-2215082 and the CMU Safety21 grant #69A3552344811. We also thank group members of Rice Wireless for their help in setting up the experiments.

A DERIVATION OF (6)

For an object at location $\mathbf{p}(\phi)$, the single-bounce system model as per (3) is

$$\tilde{\mathbf{y}}_{\text{SB}}(\omega) = \sigma_{\mathbf{p}(\phi)} \mathbf{a}_{\text{RX}}(\phi) \mathbf{a}_{\text{TX}}^{\top}(\phi) \mathbf{w}_{\text{TX}} e^{-j\omega \frac{2\|\mathbf{p}(\phi)\|_2}{c}}.$$

Substituting the above expression into (4) results in

$$\begin{aligned}\hat{\sigma}_{\mathbf{p}(\phi)} &= \frac{1}{W} \sum_{\omega} \left(\mathbf{a}_{\text{TX}}^{\top}(\phi) \mathbf{w}_{\text{TX}}\right)^* e^{j\omega \frac{2\|\mathbf{p}(\phi)\|_2}{c}} \mathbf{a}_{\text{RX}}^{\text{H}}(\phi) \tilde{\mathbf{y}}_{\text{SB}}(\omega) \\ &= \sigma_{\mathbf{p}(\phi)} |\mathbf{a}_{\text{TX}}^{\top}(\phi) \mathbf{w}_{\text{TX}}|^2,\end{aligned}$$

which results in (6) on substituting $\mathbf{w}_{\text{TX}} = \mathbf{a}_{\text{TX}}(\theta)$ and assuming unit-norm receive array steering vector $\mathbf{a}_{\text{RX}}(\phi)$.

B PROOF OF LEMMA 4.1

Let $\hat{\mathbf{p}} = \mathbf{p} + \Delta_{\text{SB}}$ be the estimated location of the object at $\mathbf{p}$ via single-bounce adjoint inversion in (4). As per (9), the double-bounce location estimate $\hat{\mathbf{p}}'$ satisfies:

$$\|\hat{\mathbf{p}}\|_2 + \|\hat{\mathbf{p}} - \hat{\mathbf{p}}'\|_2 + \|\hat{\mathbf{p}}'\|_2 = \|\mathbf{p}\|_2 + \|\mathbf{p} - \mathbf{p}'\|_2 + \|\mathbf{p}'\|_2.$$

Substituting $\hat{\mathbf{p}}' = \mathbf{p}' + \Delta_{\text{DB}}$ and assuming $\|\mathbf{p}\|_2 \gg \|\Delta_{\text{SB}}\|_2$, $\|\mathbf{p}'\|_2 \gg \|\Delta_{\text{DB}}\|_2$, $\|\mathbf{p} - \mathbf{p}'\|_2 \gg \|\Delta_{\text{SB}} - \Delta_{\text{DB}}\|_2$, we obtain:

$$\left\langle \Delta_{\text{SB}} - \Delta_{\text{DB}}, \frac{\mathbf{p} - \mathbf{p}'}{\|\mathbf{p} - \mathbf{p}'\|_2} \right\rangle + \left\langle \Delta_{\text{SB}}, \frac{\mathbf{p}}{\|\mathbf{p}\|_2} \right\rangle + \left\langle \Delta_{\text{DB}}, \frac{\mathbf{p}'}{\|\mathbf{p}'\|_2} \right\rangle = 0,$$

which on rearranging yields Lemma 4.1.

REFERENCES

[1] Mustafa Riza Akdeniz, Yuanpeng Liu, Mathew K. Samimi, Shu Sun, Sundeep Rangan, Theodore S. Rappaport, and Elza Erkip. 2014. Millimeter Wave Channel Modeling and Cellular Capacity Evaluation. *IEEE Journal on Selected Areas in Communications* 32, 6 (2014), 1164–1179. https://doi.org/10.1109/JSAC.2014.2328154

[2] Mohammed Aladsani, Ahmed Alkhateeb, and Georgios C. Trichopoulos. 2019. Leveraging mmWave Imaging and Communications for Simultaneous Localization and Mapping. In *ICASSP 2019 - 2019 IEEE International Conference on Acoustics, Speech and Signal Processing (ICASSP)*. 4539–4543. https://doi.org/10.1109/ICASSP.2019.8682741

[3] Augusto Aubry, Antonio De Maio, and Massimo Rosamilia. 2021. Reconfigurable Intelligent Surfaces for N-LOS Radar Surveillance. *IEEE Transactions on Vehicular Technology* 70, 10 (2021), 10735–10749. https://doi.org/10.1109/TVT.2021.3102315

[4] Kang Min Bae, Hankyeol Moon, Sung-Min Sohn, and Song Min Kim. 2023. Hawkeye: Hectometer-Range Subcentimeter Localization for Large-Scale MmWave Backscatter. In *Proceedings of the 21st Annual International Conference on Mobile Systems, Applications and Services* (Helsinki, Finland) *(MobiSys '23)*. Association for Computing Machinery, New York, NY, USA, 303–316. https://doi.org/10.1145/3581791.3596869

[5] Oliver Biallawons and Joachim H. G. Ender. 2020. Virtual Multistatic Illumination by Exploitation of Multipath Propagation with Coherent MIMO Radar. In *2020 IEEE Radar Conference (RadarConf20)*. 1–5. https://doi.org/10.1109/RadarConf2043947.2020.9266650

[6] Weiyan Chen, Hongliu Yang, Xiaoyang Bi, Rong Zheng, Fusang Zhang, Peng Bao, Zhaoxin Chang, Xujun Ma, and Daqing Zhang. 2023. Environment-Aware Multi-Person Tracking in Indoor Environments with MmWave Radars. *Proc. ACM Interact. Mob. Wearable Ubiquitous Technol.* 7, 3, Article 89 (sep 2023), 29 pages. https://doi.org/10.1145/3610902

[7] Zhe Chen, Guorong Zhu, Sulei Wang, Yuedong Xu, Jie Xiong, Jin Zhao, Jun Luo, and Xin Wang. 2021. M^3M3: Multipath Assisted Wi-Fi Localization with a Single Access Point. *IEEE Transactions on Mobile Computing* 20, 2 (2021), 588–602. https://doi.org/10.1109/TMC.2019.2950315

[8] Margaret Cheney and Brett Borden. 2009. *Fundamentals of Radar Imaging*. SIAM.

[9] Daniele Faccio, Andreas Velten, and Gordon Wetzstein. 2020. Non-line-of-sight imaging. *Nature Reviews Physics* 2, 6 (2020), 318–327.

[10] Ruoyu Feng, Eddy De Greef, Maxim Rykunov, Hichem Sahli, Sofie Pollin, and André Bourdoux. 2022. Multipath Ghost Recognition for Indoor MIMO Radar. *IEEE Transactions on Geoscience and Remote Sensing* 60 (2022), 1–10. https://doi.org/10.1109/TGRS.2021.3109381

[11] Dolores Garcia, Jesus Omar Lacruz, Pablo Jiménez Mateo, and Joerg Widmer. 2020. POLAR: Passive object localization with IEEE 802.11ad using phased antenna arrays. In *IEEE INFOCOM 2020 - IEEE Conference on Computer Communications*. 1838–1847. https://doi.org/10.1109/INFOCOM41043.2020.9155383

[12] Gianluca Gennarelli and Francesco Soldovieri. 2015. Multipath Ghosts in Radar Imaging: Physical Insight and Mitigation Strategies. *IEEE Journal of Selected Topics in Applied Earth Observations and Remote Sensing* 8, 3 (2015), 1078–1086. https://doi.org/10.1109/JSTARS.2014.2363233

[13] Junfeng Guan, Sohrab Madani, Suraj Jog, Saurabh Gupta, and Haitham Hassanieh. 2020. Through Fog High-Resolution Imaging Using Millimeter Wave Radar. In *Proceedings of the IEEE/CVF Conference on Computer Vision and Pattern Recognition (CVPR)*.

[14] Junfeng Guan, Arun Paidimarri, Alberto Valdes-Garcia, and Bodhisatwa Sadhu. 2021. 3-D Imaging Using Millimeter-Wave 5G Signal Reflections. *IEEE Transactions on Microwave Theory and Techniques* 69, 6 (2021), 2936–2948. https://doi.org/10.1109/TMTT.2021.3077896

[15] Geonho Han, Junil Choi, and Robert W. Heath. 2022. Radar Imaging Based on IEEE 802.11ad Waveform in V2I Communications. *IEEE Transactions on Signal Processing* (2022), 1–16. https://doi.org/10.1109/TSP.2022.3213488

[16] Zhanjun Hao, Hao Yan, Xiaochao Dang, Zhongyu Ma, Peng Jin, and Wenze Ke. 2022. Millimeter-Wave Radar Localization Using Indoor Multipath Effect. *Sensors* 22, 15 (2022). https://doi.org/10.3390/s22155671

[17] Texas Instruments. 2019. AWR1843 single-chip mmWave radar. https://www.ti.com/tool/AWR1843BOOST

[18] Texas Instruments. 2019. AWR2243 four-chip cascade mmWave radar. https://www.ti.com/tool/TIDEP-01012

[19] Ish Kumar Jain, Raghav Subbaraman, Tejas Harekrishna Sadarahalli, Xiangwei Shao, Hou-Wei Lin, and Dinesh Bharadia. 2020. MMobile: Building a MmWave Testbed to Evaluate and Address Mobility Effects. In *Proceedings of the 4th ACM Workshop on Millimeter-Wave Networks and Sensing Systems* (London, United Kingdom) *(mmNets'20)*. Association for Computing Machinery, New York, NY, USA, Article 4, 6 pages. https://doi.org/10.1145/3412060.3418433

[20] Shouhei Kidera, Takuya Sakamoto, and Toru Sato. 2011. Extended Imaging Algorithm Based on Aperture Synthesis With Double-Scattered Waves for UWB Radars. *IEEE Transactions on Geoscience and Remote Sensing* 49, 12 (2011), 5128–5139. https://doi.org/10.1109/TGRS.2011.2158108

[21] Michael Leigsnering, Moeness Amin, Fauzia Ahmad, and Abdelhak M. Zoubir. 2014. Multipath Exploitation and Suppression for SAR Imaging of Building Interiors: An overview of recent advances. *IEEE Signal Processing Magazine* 31, 4 (2014), 110–119. https://doi.org/10.1109/MSP.2014.2312203

[22] Ze Li, Zengshan Tian, Zhongchun Wang, and Zhenyuan Zhang. 2021. Multipath-Assisted Indoor Localization Using a Single Receiver. *IEEE Sensors Journal* 21, 1 (2021), 692–705. https://doi.org/10.1109/JSEN.2020.3012786

[23] Jaime Lien, Nicholas Gillian, M. Emre Karagozler, Patrick Amihood, Carsten Schwesig, Erik Olson, Hakim Raja, and Ivan Poupyrev. 2016. Soli: Ubiquitous Gesture Sensing with Millimeter Wave Radar. *ACM Trans. Graph.* 35, 4, Article 142 (jul 2016), 19 pages. https://doi.org/10.1145/2897824.2925953

[24] David B. Lindell, Gordon Wetzstein, and Vladlen Koltun. 2019. Acoustic Non-Line-Of-Sight Imaging. In *Proceedings of the IEEE/CVF Conference on Computer Vision and Pattern Recognition (CVPR)*.

[25] David B. Lindell, Gordon Wetzstein, and Matthew O'Toole. 2019. Wave-Based Non-Line-of-Sight Imaging Using Fast f-k Migration. *ACM Trans. Graph.* 38, 4, Article 116 (jul 2019), 13 pages. https://doi.org/10.1145/3306346.3322937

[26] Chris Xiaoxuan Lu, Stefano Rosa, Peijun Zhao, Bing Wang, Changhao Chen, John A. Stankovic, Niki Trigoni, and Andrew Markham. 2020. See through Smoke: Robust Indoor Mapping with Low-Cost MmWave Radar. In *Proceedings of the 18th International Conference on Mobile Systems, Applications, and Services* (Toronto, Ontario, Canada) *(MobiSys '20)*. Association for Computing Machinery, New York, NY, USA, 14–27. https://doi.org/10.1145/3386901.3388945

[27] Nishant Mehrotra, Divyanshu Pandey, Upamanyu Madhow, Yasamin Mostofi, and Ashutosh Sabharwal. 2024. Instantaneous Velocity Vector Estimation Using a Single MIMO Radar Via Multi-Bounce Scattering. In *2024 IEEE Conference on Computational Imaging Using Synthetic Apertures (CISA)*. 1–5. https://doi.org/10.1109/CISA60639.2024.10576593

[28] Nishant Mehrotra and Ashutosh Sabharwal. 2022. When Does Multipath Improve Imaging Resolution? *IEEE Journal on Selected Areas in Information Theory* 3, 1 (2022), 135–146.

[29] Kaitao Meng, Qingqing Wu, Robert Schober, and Wen Chen. 2022. Intelligent Reflecting Surface Enabled Multi-Target Sensing. *IEEE*

Transactions on Communications 70, 12 (2022), 8313–8330. https://doi.org/10.1109/TCOMM.2022.3217564

[30] Vishal M. Patel, Joseph N. Mait, Dennis W. Prather, and Abigail S. Hedden. 2016. Computational Millimeter Wave Imaging: Problems, progress, and prospects. *IEEE Signal Processing Magazine* 33, 5 (2016), 109–118. https://doi.org/10.1109/MSP.2016.2581206

[31] Andreas Pedross-Engel, Claire M. Watts, and Matthew S. Reynolds. 2020. High-Throughput 3-D Millimeter-Wave Imaging of Packaged Goods : (Invited Paper). In *2020 IEEE Radar Conference (RadarConf20)*. 1–6. https://doi.org/10.1109/RadarConf2043947.2020.9266489

[32] Akarsh Prabhakara, Tao Jin, Arnav Das, Gantavya Bhatt, Lilly Kumari, Elahe Soltanaghai, Jeff Bilmes, Swarun Kumar, and Anthony Rowe. 2023. High Resolution Point Clouds from mmWave Radar. In *2023 IEEE International Conference on Robotics and Automation (ICRA)*. 4135–4142. https://doi.org/10.1109/ICRA48891.2023.10161429

[33] Akarsh Prabhakara, Vaibhav Singh, Swarun Kumar, and Anthony Rowe. 2020. Osprey: A MmWave Approach to Tire Wear Sensing. In *Proceedings of the 18th International Conference on Mobile Systems, Applications, and Services* (Toronto, Ontario, Canada) *(MobiSys '20)*. Association for Computing Machinery, New York, NY, USA, 28–41. https://doi.org/10.1145/3386901.3389031

[34] Kun Qian, Zhaoyuan He, and Xinyu Zhang. 2020. 3D Point Cloud Generation with Millimeter-Wave Radar. *Proc. ACM Interact. Mob. Wearable Ubiquitous Technol.* 4, 4, Article 148 (Dec 2020), 23 pages. https://doi.org/10.1145/3432221

[35] Hermann Rohling. 2011. Ordered Statistic CFAR Technique - An Overview. In *2011 12th International Radar Symposium (IRS)*. 631–638.

[36] Nicolas Scheiner, Florian Kraus, Fangyin Wei, Buu Phan, Fahim Mannan, Nils Appenrodt, Werner Ritter, Jurgen Dickmann, Klaus Dietmayer, Bernhard Sick, and Felix Heide. 2020. Seeing Around Street Corners: Non-Line-of-Sight Detection and Tracking In-the-Wild Using Doppler Radar. In *Proceedings of the IEEE/CVF Conference on Computer Vision and Pattern Recognition (CVPR)*.

[37] D.M. Sheen, D.L. McMakin, and T.E. Hall. 2001. Three-Dimensional Millimeter-Wave Imaging for Concealed Weapon Detection. *IEEE Transactions on Microwave Theory and Techniques* 49, 9 (2001), 1581–1592. https://doi.org/10.1109/22.942570

[38] Raffaele Solimene, Ilaria Catapano, Gianluca Gennarelli, Antonio Cuccaro, Angela Dell'Aversano, and Francesco Soldovieri. 2014. SAR Imaging Algorithms and Some Unconventional Applications: A unified mathematical overview. *IEEE Signal Processing Magazine* 31, 4 (2014), 90–98. https://doi.org/10.1109/MSP.2014.2311271

[39] Quan Tang, Jun Li, Lingyu Wang, Yong Jia, and Guolong Cui. 2022. Multipath Imaging for NLOS Targets Behind an L-Shaped Corner With Single-Channel UWB Radar. *IEEE Sensors Journal* 22, 2 (2022), 1531–1540. https://doi.org/10.1109/JSEN.2021.3131665

[40] Deepak Vasisht, Swarun Kumar, and Dina Katabi. 2016. Decimeter-level localization with a single WiFi access point. In *Proceedings of the 13th Usenix Conference on Networked Systems Design and Implementation* (Santa Clara, CA) *(NSDI'16)*. USENIX Association, USA, 165–178.

[41] Andreas Velten, Thomas Willwacher, Otkrist Gupta, Ashok Veeraraghavan, Moungi G Bawendi, and Ramesh Raskar. 2012. Recovering three-dimensional shape around a corner using ultrafast time-of-flight imaging. *Nature communications* 3, 1 (2012), 745.

[42] Samuel Viegas, João R. Reis, Telmo R. Fernandes, and Rafael F. S. Caldeirinha. 2023. 4D MIMO Radar with 360° field of view: a practical validation. In *2023 International Wireless Communications and Mobile Computing (IWCMC)*. 757–762. https://doi.org/10.1109/IWCMC58020.2023.10182690

[43] Jue Wang and Dina Katabi. 2013. Dude, where's my card? RFID positioning that works with multipath and non-line of sight. In *Proceedings of the ACM SIGCOMM 2013 Conference on SIGCOMM* (Hong Kong, China) *(SIGCOMM '13)*. Association for Computing Machinery, New York, NY, USA, 51–62. https://doi.org/10.1145/2486001.2486029

[44] Shunjun Wei, Jinshan Wei, Xinyuan Liu, Mou Wang, Shan Liu, Fan Fan, Xiaoling Zhang, Jun Shi, and Guolong Cui. 2022. Nonline-of-Sight 3-D Imaging Using Millimeter-Wave Radar. *IEEE Transactions on Geoscience and Remote Sensing* 60 (2022), 1–18. https://doi.org/10.1109/TGRS.2021.3112579

[45] Teng Wei, Anfu Zhou, and Xinyu Zhang. 2017. Facilitating Robust 60 GHz Network Deployment By Sensing Ambient Reflectors. In *14th USENIX Symposium on Networked Systems Design and Implementation (NSDI 17)*. USENIX Association, Boston, MA, 213–226. https://www.usenix.org/conference/nsdi17/technical-sessions/presentation/wei-teng

[46] Timothy Woodford, Xinyu Zhang, Eugene Chai, and Karthikeyan Sundaresan. 2022. Mosaic: Leveraging Diverse Reflector Geometries for Omnidirectional Around-Corner Automotive Radar. In *Proceedings of the 20th Annual International Conference on Mobile Systems, Applications and Services* (Portland, Oregon) *(MobiSys '22)*. Association for Computing Machinery, New York, NY, USA, 155–167. https://doi.org/10.1145/3498361.3538944

[47] Dianhan Xie, Xudong Wang, and Aimin Tang. 2022. MetaSight: Localizing Blocked RFID Objects by Modulating NLOS Signals via Metasurfaces. In *Proceedings of the 20th Annual International Conference on Mobile Systems, Applications and Services* (Portland, Oregon) *(MobiSys '22)*. Association for Computing Machinery, New York, NY, USA, 504–516. https://doi.org/10.1145/3498361.3538947

[48] Qian Yang, Hengxin Wu, Qianyi Huang, Jin Zhang, Hao Chen, Weichao Li, Xiaofeng Tao, and Qian Zhang. 2023. Side-Lobe Can Know More: Towards Simultaneous Communication and Sensing for MmWave. *Proc. ACM Interact. Mob. Wearable Ubiquitous Technol.* 6, 4, Article 191 (Jan 2023), 34 pages. https://doi.org/10.1145/3569498

[49] Keisuke Yoneda, Naoya Hashimoto, Ryo Yanase, Mohammad Aldibaja, and Naoki Suganuma. 2018. Vehicle Localization using 76GHz Omnidirectional Millimeter-Wave Radar for Winter Automated Driving. In *2018 IEEE Intelligent Vehicles Symposium (IV)*. 971–977. https://doi.org/10.1109/IVS.2018.8500378

[50] Shichao Yue, Hao He, Peng Cao, Kaiwen Zha, Masayuki Koizumi, and Dina Katabi. 2022. CornerRadar: RF-Based Indoor Localization Around Corners. *Proc. ACM Interact. Mob. Wearable Ubiquitous Technol.* 6, 1, Article 34 (Mar 2022), 24 pages. https://doi.org/10.1145/3517226

[51] Wei Zhao and Rong Zheng. 2023. MARS: A MmWave Rotating Synthetic Aperture Radar System for Indoor Imaging. In *Proceedings of the First ACM Workshop on MmWave Sensing Systems and Applications* (Istanbul, Turkiye) *(mmWave '23)*. Association for Computing Machinery, New York, NY, USA, 8–13. https://doi.org/10.1145/3628357.3629709

[52] Yanzi Zhu, Yuanshun Yao, Ben Y. Zhao, and Haitao Zheng. 2017. Object Recognition and Navigation Using a Single Networking Device. In *Proceedings of the 15th Annual International Conference on Mobile Systems, Applications, and Services* (Niagara Falls, New York, USA) *(MobiSys '17)*. Association for Computing Machinery, New York, NY, USA, 265–277. https://doi.org/10.1145/3081333.3081339

[53] Yanzi Zhu, Yibo Zhu, Ben Y. Zhao, and Haitao Zheng. 2015. Reusing 60GHz Radios for Mobile Radar Imaging. In *Proceedings of the 21st Annual International Conference on Mobile Computing and Networking* (Paris, France) *(MobiCom '15)*. Association for Computing Machinery, New York, NY, USA, 103–116. https://doi.org/10.1145/2789168.2790112